Chiro-electrooptical Triggers with Multifunctional Active Dielectric Layer of Field Effect Electronic for Logic Discretion

Moon Jong Han, Minkyu Kim, and Vladimir V. Tsukruk*

School of Materials Science and Engineering, Georgia Institute of Technology, Atlanta, GA 30332, USA

* Tel: 1-404-894-6081; e-mail: Vladimir@mse.gatech.edu

Abstract

We suggest that chiral photonic bio-enabled field-effect transistors can pave the base for next-generation optoelectronic processings including quantum-like coding for encryption as well as integrated multi-level logic circuits. Despite recent advances, thin-film electronic elements for encryption applications with reconfigurable and multi-valued logic systems, are not reported. Herein, highly secure optoelectronic encryption logic elements are demonstrated by facilitating humidity-sensitive chiral pitch of chiral nematic organization of cellulose nanocrystals (CNCs) as active dielectric nanolayer combined with printed-in organic semiconducting channels. By adding the different concentration of salt solutions into the photonically-active chiral nematic layer, the photonic band gap shift can be tailored to facilitate distinguishable and quantized electric signal logic triggers with repetitive changes of humidity, voltage, and the polarization state of the incident light. The convergence between photonic and electronic properties into the multi-valued logic system can provide optoelectronic counterfeiting, imaging, and information processing with high-level multi-level logic nodes. As a proof-of-concept, the integrated circuits sensing of circularly polarized light and humidity are demonstrated as a physically unclonable functional bi-material field-effect elements with high-level logic.

KEYWORDS: **circularly polarized processing; bio-organic field-effect transistors; multi-valued logic systems; photonic cellulose nanocrystals; multifunctional logic electronics; multi-level optical communications;**

Introduction

In nature, unique structure colors appear in the skin of various living things, including beetles, birds, and fishes, mainly due to the complex hierarchical structure of organic and biological components. [1,2,3] Interestingly, some elements of the biological entities consist of chiral supramolecular structures, where the selective light reflection generates under different circularly polarized light (CPL).[4] Such unique photonic crystal structure over a large scale allows them to adjust in dynamic environments through optical communications, including adaptive appearance and camouflaging, found in the palatopods, cephalopods, crickets, or bees. [5,6,7,8] Cases of information exchange via linear and circular can be found in modern information technology[9,10,11,12] and spintronics effects. [13] Nature-inspired chiral architectures have been applied to smart materials and sensors to modulate stimulus-response behavior through selective light reflection and diffraction as controlled by environmental conditions such as humidity, heat, stress, current, and pH. [14,15,16,17,18,19] Such chiral assembled structures can be realized with crystalline TiO_2 microspheres,[20] thiol-acrylate chemistry,[21] and semi-interpenetrating polymer networks.[22]

However, most chiral structures are ineffective in converting changes of chiral nematic structures into readable output values. On the other hand, chiral materials from cellulose nanocrystals (CNCs) can be fabricated by an evaporation-induced self-assembly process with pitch length controlled by processing conditions.[23,24,25,26] The high density of the hydroxyl group on the surface of the CNCs can generate a mesoporous structure with channels and bonding sites that can be adjusted in accordance with the chiral nematic structure,[27] which can be alternately adjusted to the helical pitch induced by the stimulus, resulting in significant color modulation. Therefore, CNC films and coating techniques have been utilized as templates to develop humidity,[28] light,[29] stress,[30] and magnetic-responsive materials.[31] Adjustable helical pitches rely heavily on external stimuli, but practical implementation of device-related principles remains a significant challenge in the field.

Here, we demonstrate that a combination of the responsive active dielectric layer of chiral CNC films and opto-electrically triggered semiconducting conjugated channels encoded by circular polarization of light and relative humidity provides an executable design for accessing information that can be decoded by thin film electronic devices such as organic field-effect transistors (OFETs). In this design, discrete optoelectrical signals can be read out and triggered by the polarization state of the incident light, voltage, and humidity conditions. The individual

CNC-based bio-organic field-effect transistors (BOFETs) can be triggered by on/off gate voltage (V_{GS}), polarization states of light, and humidity conditions, resulting in quaternary logic systems operation. Finally, a high-level 13-digit system is demonstrated by introducing an integrated inverter comprising p- and n-type organic semiconductors. By converting the distinguishable optoelectrical signals to Alphabet letters, number substitution cypher, an elaborate optical communication, even advanced cryptographic techniques are suggested, where external stimuli elevate the coded information space beyond traditional digital processing.

Results and Discussion

Fabrication of Encryption Logic

Fig. 1a–d shows an underlying fabrication process of the active dielectric element and optoelectrical device and a flow diagram of the optical communication with encrypting information based on treated CNC films (see fabrication procedure in the Experimental Section). Briefly, an indium tin oxide (ITO)-deposited glass acts, acting as the substrate and a standard gate electrode, is attached to the Petri dish. Under a controlled condition (25% relative humidity (RH) and T = 25 °C) for one day, evaporation-induced self-assembly (EISA) generates CNC films with the chiral nematic organization.[32,33] The dry films were subsequently subjected to the dropping of different NaCl solutions to induce different photonic bandgaps (Fig. 1a). CNC layers show iridescence and selective reflection and transmission of CPL, owing to the intrinsic chirality of left-handed twisted supramolecular structures.[34] Thus, LCPL is reflected, whereas RCPL is transmitted.

The disguisable photonic pattern of responsive photonic materials is realized depending on the salt concentration (right of Fig. 1a), due to the salt-induced change of helical pitch.[35,36,37] Because CNCs and NaCl salt has contrasting water absorption abilities, the concentration of NaCl tunes the precise reflection color of NaCl-dropped CNC films, such as blue, green, and reddish coloration. The distinct photonic bandgaps tailor polarization state-dependent optoelectrical signals of BOFETs-based multi-valued logic systems (MVLS) (Fig. 1b). Overall, by combining relative humidity (H), salt concentration (S), and the wavelength (W) and polarization state (P) of

the incident light - dependent chiral pitch modulation of CNC films, we design the bio multi-valued logic system (Fig. 1c).
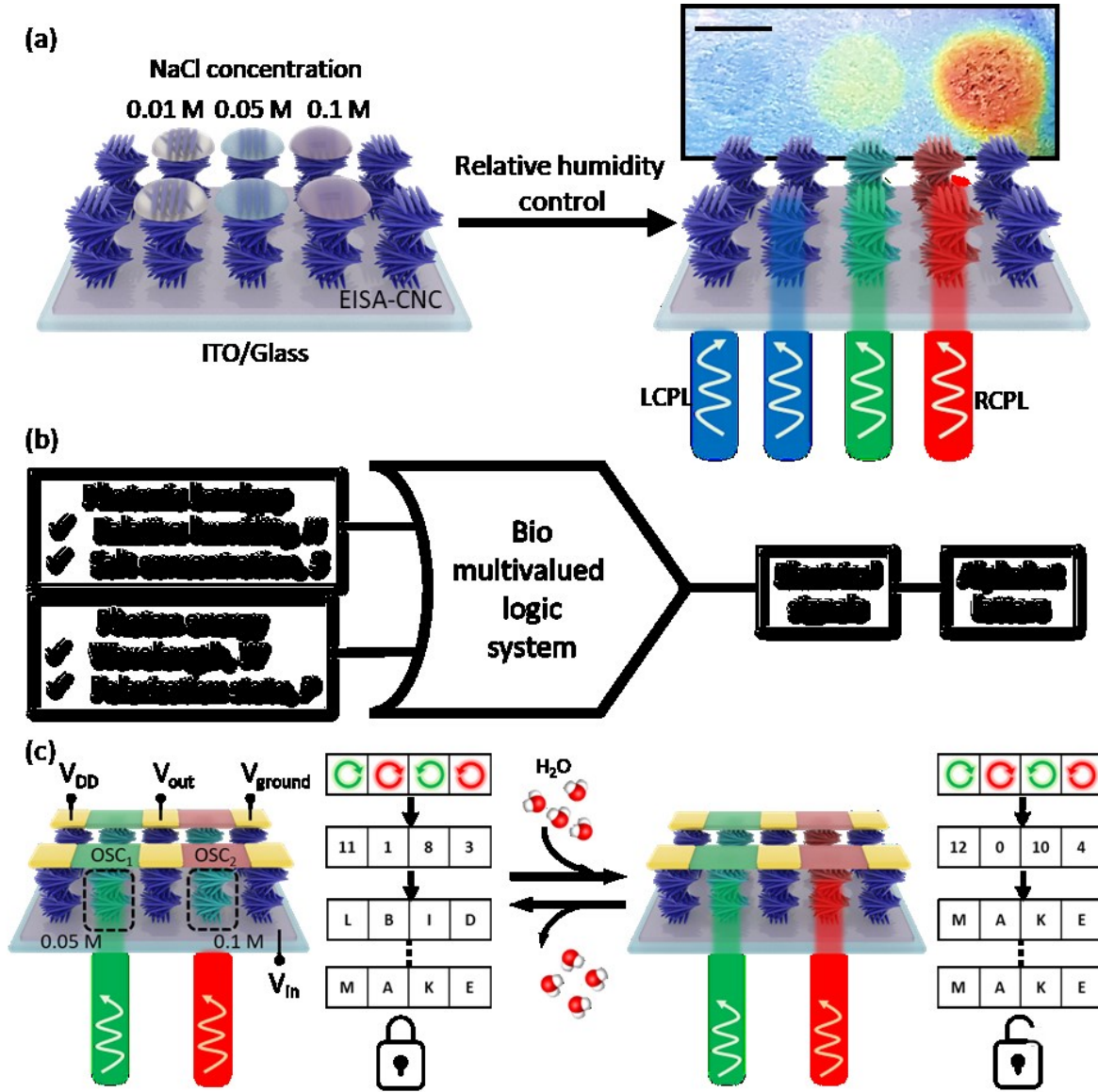

Figure 1. Multivalued logic thin-film elements with encryption. (a) Evaporation-induced self-assembed (EISA) CNC film onto the ITO/glass substrate. By precise dropping of NaCl solutions, the chiral pitch of CNC is tuned by relative humidity control (scale bar is 1mm). (b) Graphical symbol of a bio multivalued logic system triggered by photonic bandgap (relative humidity, H and salt concentration, S) and photon energy (wavelength, W and polarization state, P), decoding electrical signals with following converted alphabet letters. (c) Optical communication based on the integrated circuits enabled active chiral bio-dielectric layers. The specific inputs afford optical communication, transiting "MAKE" signals with encryption by tuning H within the system.

Therefore, conversion of discrete chiro-optoelectrical signals to the coded optical communication and decryption becomes possible (Fig. 1c). By additional deposition of gold electrodes and organic

semiconductors (OSCs) by thermal evaporation and ink-jet printing, respectively, the completed integrated circuits are fabricated (Fig. S1).[38,39]

Morphology and optical properties of CNC films

The atomic force microscopy (AFM) images revealed the morphology of the CNC films under different salt concentrations, such as 0.05 (Fig. 2b) and 0.1 M (Fig. 2c), of the CNC films to be similar except for the 5 M case (Fig. 2a-d). AFM images confirm the ordered chiral nematic configuration transition to a completely segregated and disordered organization as concentration reaches 5 M. The quantitative analysis orientational analysis of the corresponding AFM images allows for calculation of azimuthal distribution and 2D orientational parameter (Fig. S2).[40]
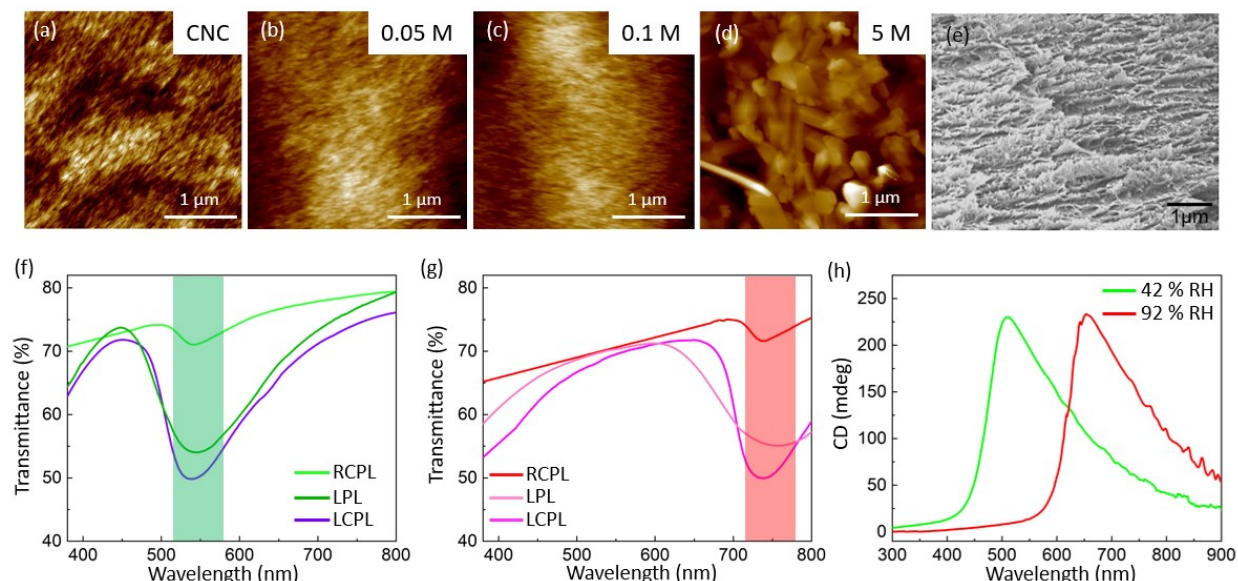
Figure 2. Structural characterization of active photonic CNC film with NaCl deposition. (a-d) AFM and (e) SEM image of CNC film. Especially, (b) 0.05 (c) 0.1 (d) 5 M of NaCl solution deposition onto the CNC film. UV-vis transmittance of CNC film at (f) 42 and (g) 92 % RH condition with RCPL, LPL, and LCPL polarization state. (h) CD spectra of CNC film at 42 and 92 % RH condition.

Corresponding molecular orientation order parameter within microscopic surface areas is very high, 0.92, 0.91, 0.89, pristine, 0.05, 0.1 M concentration and very low, 0.12 for 5 M, respectively. The twisted Bouligand morphology for loq salt conncentration, a signature of the chiral nematic organization, was also confirmed by scanning electron microscopy (SEM) (Fig. 2e).

CPL transmission spectra show the different CNC films show changes in photonic properties under different conditions (Fig. 2f, g), where the polarization of the incident light applied was left-handed circular polarized light (LCPL), linearly polarized light (LPL), and right-

handed polarized light (RCPL) in addition to unpolarized light and dark conditions. As expected, RCPL shows an increase in transmittance in the range between 80 and 90 % with respect to the measured wavelength region. Compared with the 42 % RH condition, the salt treatment induces a change of the helical pitch with a redshift of the photonic bandgap (Fig. 2g). Linearly polarized light transmittance profile is intermediate between the RCPL and LCPL transmission (Fig. S3). The pitch length (P) is calculated from these spectra to the equation:[41,42]

$$\lambda_{reflected} = n_{avg} P sin\theta_i \tag{1}$$

with the reflected wavelength ($\lambda_{reflected}$), the average refractive index (n_{avg}), the pitch length of a full cholesteric rotation (P), and the angle between the incident light and the helical axis of CNC film (θ_i). From this equation, one can obtain the pitch length with increasing RH by using an average refractive index of $n_{ave}= 1.5$.[43] An increase in pitch length with humidity indicates the gradual swelling of the films by steady water adsorption and diffusion into CNC porous matrix from about 400 nm at 42% to 480 nm at 92 % RH.   Furthermore, the CNC films with helical chiral nematic organization show characteristic positive peaks at circular dichroism (CD) spectra with a distinct red shift at higher humidity from 520 nm to 700 nm (Fig. 2h),[44,45] indicating preservation of left-handed chirality of self-assembled CNC structures at all humidity conditions.

Individual BOFET element for photonic bandgap-controlled logic

To realize the discrete optoelectrical signal output element based on the active bio-chiral dielectric layer discussed above, the p-and n-type organic semiconductors (OSCs), PBTTT-C14 and ITIC-F, respectively, were printed for the individual BOFET element as patterned channels (Fig. S4). These compounds exhibit different strong absorption peaks around 550 and 740 nm, respectively, guaranteeing independent integrated circuits operation (Fig. S5).

The ink-jet deposited OSC channels show low surface roughness, R_q of 2.0 ~ 2.9 (1×1 μm^2 surface area), and very fine, nanoscale (< 50 nm) grain dimensions with a thickness of ~ 55 nm (Fig. S6). Thus, they are capable of effective responses under the incident lights without light losses, therefore, affording efficient multi-stimuli responsive active channels (Fig. 1c).

The humidity-controlled changes in light transmittance within the BOFET element control chiro-opto-electrical signal under variable conditions (Fig. 3a, b). For low RH conditions, corresponding to the greenish reflection color's chiral pitch (Fig. 3a), the transmittance of the

incident green light (550 nm LED) increases in the LCPL, LPL, and RCPL sequence. Humidity increases result in reddish coloration, tuning the negligible transmittance of three polarization states of the incident light (Fig. 3b).

Depending on the RH and the subsequent chiral pitch of CNC films, the transmittance of the different polarized lights tunes the chiro-opto-electrical outputs of the individual BOFET elements (Fig. 3c,d). Based on the p-type OSC properties of PBTTT-C14, the transfer curves (drain current vs gate voltage) clearly reveal the dramatic change in drain current for different light conditions (Fig. 3c-d). At the same time, it adjusts the transmitted light through the CNC films, directly affecting the resultant meaningful light intensities to the OSC channels. Each LED wavelength is 550 (green) and 730 nm (red), matching the absorbance bands of PBTTT-C14 and ITIC-F, respectively. By switching the polarization state in the order of dark, LCPL, LPL, and RCPL, the high transmittance of light triggers different electrical signal outputs (Fig. 3c, d), generating high photo-generated charges within the OSC channel. The higher effective light intensity through the higher transmitted photonic CNC layer by tuning the polarization condition, the more shifts of the threshold voltage (V_{th}) to the negative and positive directions, opposite for ITIC-F and PBTTT-C14 conditions, respectively, with the significant $|I_{DS}|$ output increase. For the higher RH conditions, the negligible transmittance difference affords a similar transfer characterization by tuning the incident polarization conditions, where an increase of on-current generates, resulting from the high accumulated charges at the OSC/CNC interface (Fig. S7).

The humidity/polarization responsive behavior facilitates quaternary logic behavior (Fig. 3e, f). The transient responses of on/off V_{GS} (V_{on} = - 2V and V_{off} = 1 V) and under light with different polarization conditions with 10 s intervals is investigated (Fig. 3e, f). For low RH condition (Fig. 3e), 42 % RH, due to the tuned effective transmittance intensity of light, the currents are modulated depending on the polarization state of light. The logic "0", "1", "2", and "3" correspond to each chiro-opto-electrical condition as long as the current outputs don't exceed 1 order. At higher humidity (Fig. 3f), the overall currents increase compared with low RH condition and show negligible differences regardless of the incident light polarization states, inducing the same "3" logic value in the system.

For the ITIC-F layer (Fig. S8), the 730 nm LED modulates the chiro-opto-electrical signals with the independent RH conditions. Due to the polarization-dependent effective transmittance intensity of 730 nm light through the chiral photonic CNC layer, the opposite results are
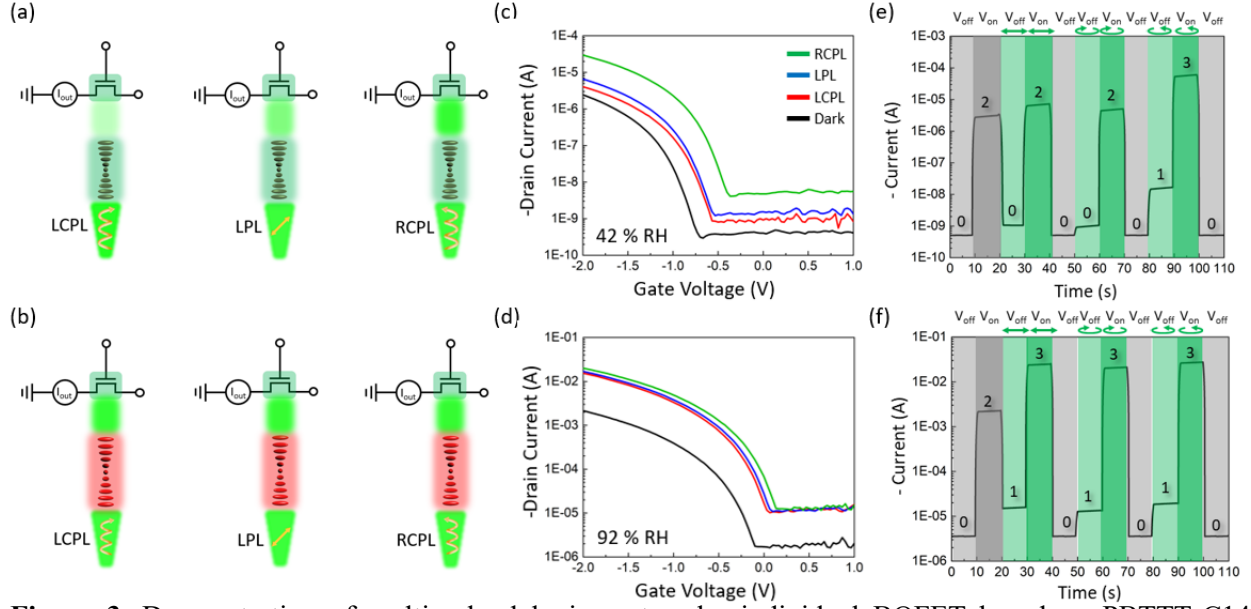
Figure 3. Demonstration of multi-valued logic system by individual BOFET based on PBTTT-C14. Modulation of the incident light through CNC film by varying polarization state at (a) 42 and (b) 92 % RH. (c) Transfer characterization of BOFET at (c) 42 and (d) 92 % RH, triggered by polarization state. Transient response of quaternary logic system by voltage, RH and polarization of light at (e) 42 and (f) 92 % RH.

demonstrated. For low RH case, the same "2" logic value appears regardless of the polarization conditions; however, the "3" logic state generates for high RH cases under LPL and LCPL conditions. Observed changes in drain current span a very wide range from 0.5 nA to 100 μA and from 50 μA to 50 mA at low and high humidity, respectively (Fig. 3e, f).

The chiroptical functionality of the individual BOFET based on PBTTT-C14 is evaluated quantitatively by using a dissymmetry factor of responsivity (g_R):[46]

$$g_R = \frac{2(R_{RCPL} - R_{LCPL})}{R_{RCPL} + R_{LCPL}} \qquad (2)$$

where R_{RCPL} and R_{LCPL} indicate the responsivities under the RCPL and LCPL exposure, respectively. The average g_R values were extracted to be + 1.63 and 0.52, depending on 42 and 92 % RH conditions, respectively, which is comparable to the value of the previously reported chiroptical electronics.[47,48] The g_R of the ITIC-F BOFETs exhibit + 0.26 and 1.52 for 42 and 92 % RH conditions, respectively.

For the performance stability evaluation, the BOFETs are measured under bias stress as a function of RH, such as 42 and 92 % RH and light irradiation of RCPL (Fig. S9). The normalized drain current ($I_{DS}(t)/I_{DS}(0)$) of the time-dependent variation is explored, where $I_{DS}(t)$ is the drain current at time t and $I_{DS}(0)$ is the drain current at t = 0. The bias-stress is constant with $V_{GS} = V_{DS}$

8

= - 2 V for 1 h at different RH conditions. The normal decay of I_{DS} is measured under both 42 and 92 % RH conditions . As the concentration of water molecules at the OSC/dielectric layer interface increases, the strength of local field also increases and the dipoles are polarized must faster, resulting in the highly sensitive and fast decay of I_{DS} related to the field-induced charge trapping or oxygen vacancies at the semiconductor/dielectric layer interface.[49,50] In detail, at the highest humidity of 92 % RH, I_{DS} decreased by 33 % within 3000 s and maintained a constant level in the remaining time of the bias stress application.

The RH dependency of the optoelectrical properties are based on both charge trapping and dielectric polarization in the FETs.[51,52] As RH increases, weaker charge trapping and stronger polarization cause an increasing recombination rate with a shorter time reaching the equilibrium state, leading to a faster photocurrent decay and smaller saturated photocurrent (Fig. S9).[53] As a representative example of the optoelectrical measurement of BOFET, RCPL illumination has been applied. For 92 % RH condition, the time-dependent I_{DS} of RCPL case decreased by 24 % within 2400 s, which indicates 1.4 and 1.3 times lower I_{DS} and shorter time reaching saturation region, compared to the dark condition.

Bi-materials logic nodes with photonic energy and bandgap tuning

Note that the light transmittance through the active dielectric layers with two different OSCs can be modulated by the photonic bandgap (H) of the chiral photonic layer and the effective absorbed photon energy (W) of OSC channels with polarization state (P) of the incident light as well as on/off voltage (V) of V_{in} (Fig. 4). The integrated inverter circuits consisting of PBTTT-C14 and ITIC-F OSC channels are demonstrated (Fig. 4a). The H, E, P, and V-dependent chiro-optoelectrical properties for the bio-multi-valued logic system (MVLS) are shown in the Fig. 4b,c. The H controls the transmittance of light through CNC film under applying the different W, generating distinct V_{out} within the voltage transfer curves (VTC), which can be utilized for MVL applications. The inverter shifts within the VTC toward the negative V_{in}, which is caused by photo-generated charging with an increase in conductance of each OSCs channel.[54,55]   For example, at 42 % RH, the 730 nm wavelength region exhibit relatively high transmittance of the incident light

compared with the 550 nm region (Fig. 2f), causing increased photo-generated charges of the ITIC-F channel than those of the PBTTT-C14 channel.
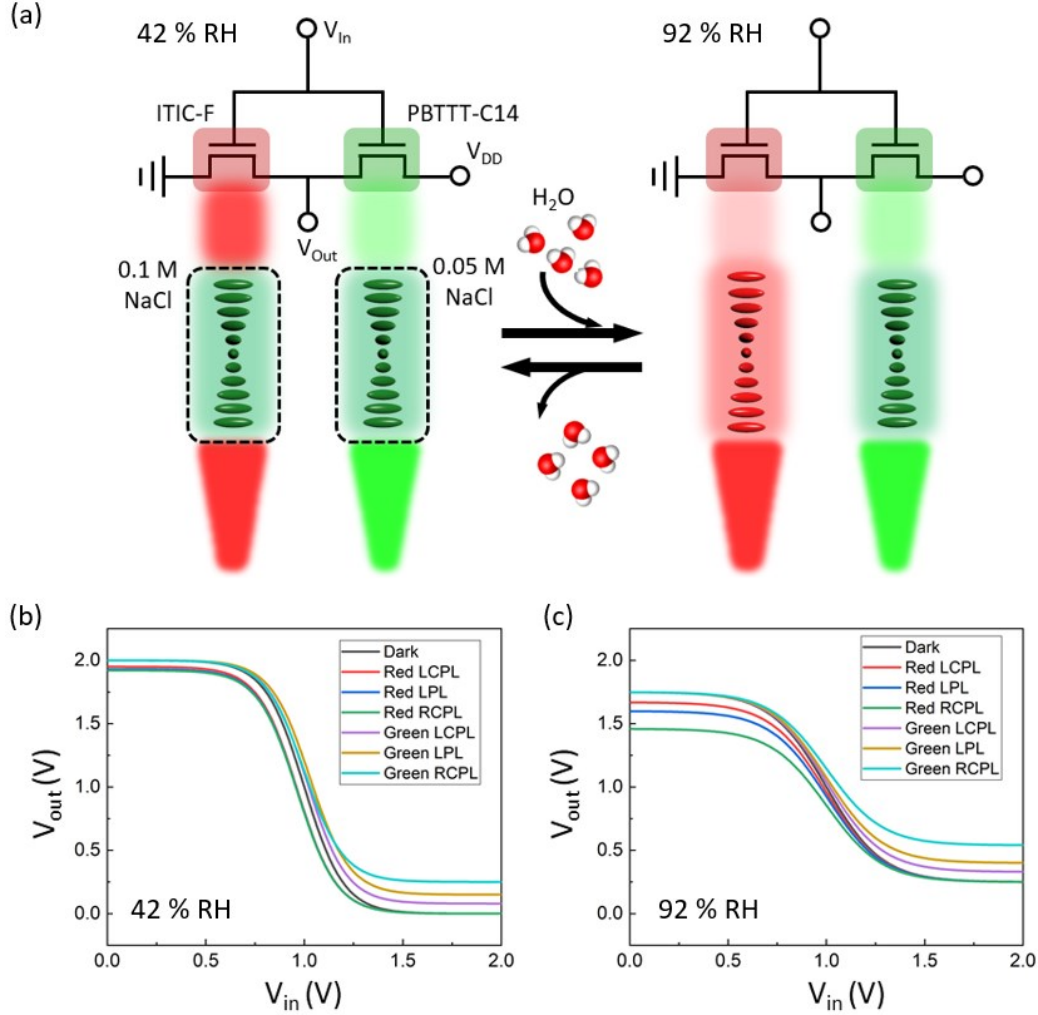
Figure 4. Design of 13 digit logic system based on salt concentration-dependent chiral pitch of active bio chiral dielectric layer. (a) Schematic illustration of the integrated inverter circuits triggered by salt concentration, humidity, and polarization state of the incident of light. Voltage transfer curves of the inverters at (b) low and (c) high RH condition by varying polarization of light. The active transmittance of light through CNC layer, triggered by dark, LCPL, LPL, and RCPL illumination with green and red light, tunes optoelectrical signals of the integrated inverter directly. Detailed transmittance degree follows the scheme in Fig. 3a, b.

By varying the conditions of the exposed LEDs, such as dark, 550, and 730 nm, the VTC moves following the positive or negative direction, respectively. We relate this phenomenon to the transition of the cross-region from the output characteristics of p-type PBTTT-C14 and n-type ITIC-F-based BOFETs along the positive direction under different W and P of the green light exposure (Fig. S10). Note that the higher transmittance of green LED at low RH and red LED at high RH conditions at which an elaborate transmittance appears in the order of dark, LCPL, LPL,

and RCPL (Fig. 3a,b). In the case of the red light case under 42 % RH, the transmitted light through the chiral photonic CNC layer is relatively high compared to that under the green light condition, resulting in effectively high photo-generated charges in the ITIC-F active layer. However, the negative shift of VTC happens, governed by the constant photo-induced charge mechanism.[54] For the 92 % RH case, the V_{out} decreases under applying low V_{in}, resulting from the output resistance decrease with the off-current increase (Fig. 3c,d). At high V_{in}, the V_{out} shows a significant increase, compared with the 42 % RH case, affected by the additional leakage current with a high concentration of water molecules. Therefore, green or red LED exposure affords the positive or negative shift within the VTC owing to the V_{th}'s positive or negative shift due to the photo charges.

Finally, the generalized reconfigurable bio-13 digit logic system is summarized in Table 1 and Fig. S11 shows the applied sequential inputs, such as *H*, *E*, *P*, and *V*. Each V_{out} as a result of the combination of three triggers corresponds to the discrete logic values of "0" ~ "12". In this system, we designate "0" corresponding to 0 ~ 0.05 V of V_{out} and the other logic states were done with 0.05 V intervals (Table 1).

Inputs			Output	Inputs			Output
Humidity	Optical	Electrical		Humidity	Optical	Electrical	
Low	Dark	V_{out}	12	High	Dark	V_{out}	10
		V_{in}	0			V_{in}	3
	Green LCPL	V_{out}	12		Green LCPL	V_{out}	10
		V_{in}	1			V_{in}	4
	Red LCPL	V_{out}	11		Red LCPL	V_{out}	9
		V_{in}	0			V_{in}	3
	Green LPL	V_{out}	12		Green LPL	V_{out}	10
		V_{in}	2			V_{in}	5
	Red LPL	V_{out}	11		Red LPL	V_{out}	8
		V_{in}	0			V_{in}	3
	Green RCPL	V_{out}	12		Green RCPL	V_{out}	10
		V_{in}	3			V_{in}	6
	Red RCPL	V_{out}	11		Red RCPL	V_{out}	7
		V_{in}	0			V_{in}	3

Table 1. Chiro-optoelectrical outputs triggered by humidity, the polarization state of the incident light, and voltage for the configuration of Fig. 4

The efficiently absorbed light through a thin dielectric layer was confirmed by the adequate electronic device performance owing to significant light selection via the chiral nematic organization. By dropping NaCl solution (0.1 M) onto CNC films, where the pristine reflection

color is red, the different chiro-optoelectrical outputs can be generated fast (Fig. S12 and Table S1).   Indeed, the rate of humidity variation can be as low as 30 ms from 20 to 80 % RH if the mass flow controller and saturated aqueous solution are in use.[56] In terms of a system composed of a humidifier and fan motor, the humidity values can be modulated from 30 to 100% RH in 15 s.[57] Also, recent research demonstrated dynamic structural color-tuning characteristics based on the cellulose composites, tuned with a relatively short response time such as a few seconds and 4 min for CNC/NaCl and CNC/polyacrylamide (PAM) case, respectively.[58,59,60]

High-level 13-digit logic elements for multiplexed optical coding and communication

Recently, we have reported the CNC composite BOFETs system, exhibiting the reconfigurable quinary logic values identically for each device array.[61] However, to realize more subdivided logic values by facilitating the chiral supramolecular structures and salt concentration (C) -dependent chiral pitch modulation of the unique biopolymer characteristics, circularly polarized lights (P) and the solution patterning of NaCl electrolyte onto the prepared CNC film have been introduced in this study in order to design higher-level readable discrete signals. Thus, based on this approach, we demonstrate reconfigurable 13-digit logic values with the potential for MVLS for elaborate optical communication with advanced encryption applications that were unreachable in previous designs.[61,62,63,64]

For optical communication, cryptographic techniques using CPL have been suggested.[65,66] Commonly, the telecommunication technique converts the blinking lights to digital information, where the more complex encryption is, the more amounts of flashing lights containing additional encrypted data increase. On the other hand, encrypted information by the polarized lights can be utilized as an effective technique to transform given information with no significant data amounts increase. As the polarization states of circularly polarized lights, σ_+ and σ_-, are modulated or vanished, the eavesdropping phenomena could appear. By utilizing an approach, such as a wireless power supply system within free space, only designated electronics can respond to the inputs. For short-distance communication between a plurality of opposing fixed devices, polarization information can be transported without waste. However, long-distance CPL communication requires constant maintenance feedback because CPL transmission through curved optic fibers generates unreliable depolarization.

Here, a proof-of-concept dynamic encryption for optical multiplexing communication is proposed by utilizing a reconfigurable 13-digit logic system (Fig. 5). For the CNC films-based BOFET elements (encrypted device), the output signals are controlled by the multiple decoding conditions (keys) such as photon energy, E (or wavelength, λ), and photon polarization, P, with both responses biased by controlled RH (H) (Fig. 5a). Through the number substitution cypher from optoelectrical signals to the Alphabet, the information decryption can be generated the secure optical communication (Fig. 5b).
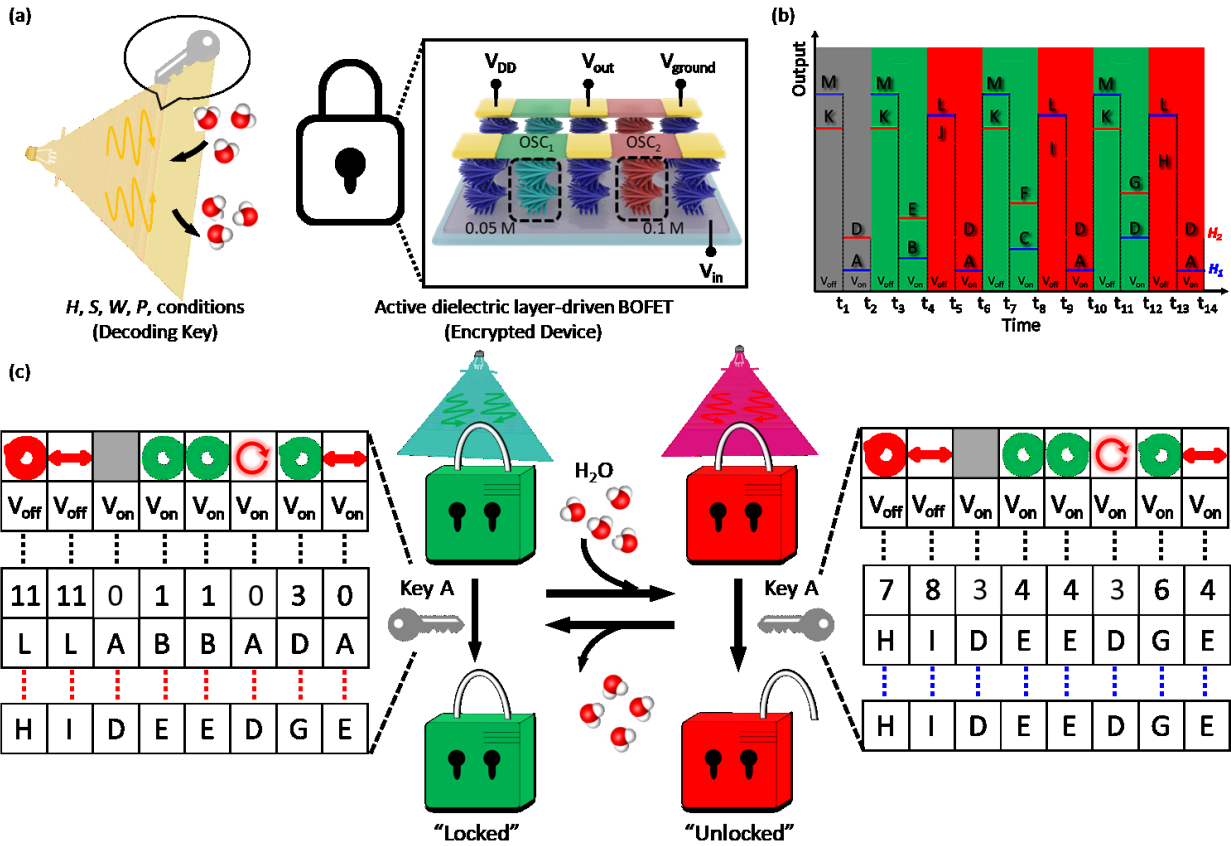
Figure 5. Chiroptical communication with encryption information by utilizing multifunctional bio-photonic materials-based BOFETs. (a) The elements of the chiro-optoelectrical communications with encryption such as decoding keys and encrypted device. (b) Alphabet letters converted by 13 V_{out} values by sequence. (c) Proof-of-concept of chiro-optoelectrical communication with decryption by applying chiro-optoelectrical triggers order, generating different letter sequence that decides the system unlocking.

In this design, the multiple diverse key inputs, such as polarization state, voltage, and humidity, are exploited as inputs/triggers for transmission channels. A sequence of the polarization state of the incident light with different wavelengths, such as dark, 550, and 730 nm, is applied for

low and high RH conditions. For example, RCPL, LPL, and LCPL polarization states, green and red incident lights, and on/off voltages are all explored for the dynamic encryption systems. The green and red locks represent low and high RH, respectively (Fig. 5c), being unlocked when an appropriate key matches the lock's underlying password.   On the basis of the chiro-optoelectrical signals of the integrated inverters display 13-digit logic (Fig. 4), each value is transformed into the Alphabet by considering the number substitution cypher, which can express the Alphabet from "A" to "M", matching with "0" to "12" (Table S2).

This deconvolution process simultaneously transmits encrypted digital information for optical communication.   The system can transmit the encrypted information and afford chiro-optoelectrical communication by detecting the lock matching with the key, which programs the photonic bandgap, absorbed photon energy of OSC layers with the polarization and on/off voltage. For example, the intended alphabetical order to be transmitted is "HIDEEDGE", but it can be transmitted by encrypting from low humidity to "LLABBADA", which can be confirmed by increasing H (Fig. 5). Overall, the 13- bit signals can be transmitted with only four different triggers by harnessing H-responsive BOFETs-based circuits, which is 7-fold more efficient than conventional single-channel optical communication at a similar readout speed.

Conclusion

In conclusion, a highly secured optoelectronic encryption dual-materials-based methodology has been suggested by facilitating humidity-sensitive chiral photonic bandgap of active dielectric nanolayers combined with light-sensitive absorption of printed-in organic conjugated channels. The consistent shift in photonic band gap can be converted into distinguishable and quantized electric signal outputs in thin-film electronic elements by combining environmental humidity, the voltage applied, and the citccular polarization of the incident light. For the individual BOFET element, the combined triggers can generate stable quaternary logic states by representing the drain currents, which depend on the channel type. Based on the corresponding variation in photo charging, the integrated inverter circuits show the complex multi-level 13-bit signal output within the voltage transfer curves, a unique multifunctional phenomenon. The standard one-kind key encrypted system shows the weakness of comparatively low-level information protection. If the encryption and plain-text data exist simultaneously, this kind of key could be estimated by

unintended invaders, and the key cannot be obtained after the decoding process. The polarization state-based encryption technique is newly developed to improve these challenges in the systems by manipulating the polarized lights, resulting in readable outputs, which provides opportunities for teleportation and dynamic encrypted systems.[67,68]

By combining different physical phenomena, the novel multi-valued logic system became capable of providing the coding-decoding ability for prospective chiro-optoelectronic counterfeiting, image coding, and external information processing with logic nodes. The integrated inverter circuits sensing circularly polarized light and controlled humidity are demonstrated as a physically unclonable functional device with coded optical communication and other low-power organic artificial light-induced encryption applications with fast "on-site" highly secure optical information coding and processing.

Methods

CNC Synthesis: CNCs were prepared by the sulfuric acid hydrolysis technique.[69] The dried wood pulp within 64 wt% sulfuric acids was stirred at 45 °C continuously. The hydrolysis process was conducted for 60 min and it was quenched by adding a tenfold volume of MiliQ Nanopure water to the solution. The diluted solution was maintained at 25 °C for 12 hr. The clear supernatant was pulled out and the precipitate was washed with the MiliQ Nanopure water by centrifugation process. The resultant solution within the dialysis tube (14 kDa molecular weight cut off) was dialyzed in contrast to deionized (DI) distilled water until the pH value of DI water became constant (~ 72 hr). The DI water was changed every 3 hr for the dialysis process. The resultant solution was centrifuged at 11,000 rpm twice. Then, the collected supernatant was sonicated by a tip-sonicator (1.2 cm diameter probe, Q700 model, QSonica) for 270 s (5 s on/off with 40% amplitude).

Fabrication of CNC layer: The UV/Ozone treatment to the hydrophobic ITO-coated glass substrate was performed for 30 min (PSD Series, Digital UV Ozone System by NOVASCAN) to prepare the uniform spread of CNC solution. Next, the substrate was adhered by double-sided tape to the cleaned round-shaped Petri dish (diameter: ~ 60 mm). The 12 mL of CNC aqueous solution (1 wt %) was poured, where chiral photonic film generates by evaporation-induced self-assembly during solvent drying for ~ 2 days within a maintained condition (25% RH, T = 25 °C). Each 1 µL

from 0.05, 0.1, and 5 M NaCl (Sigma Aldrich) aqueous solution was further dropped into the prepared CNC film to change the photonic bandgap.

The humidity modulation was done by putting the prepared samples into the humidity-controllable chambers. Each 42 and 92% RH, measured by a Cole-Parmer hygrometer, were prepared by a saturated solution of potassium carbonate (K_2CO_3) and potassium nitrate (KNO_3), respectively.[70] The humidity-conditioned polystyrene (2.5 cm × 2.5 cm × 2.5 cm, Ted Pella) was placed into the borosilicate glass (8 × 6.5 × 3 inch, MICRO), which was sealed by a parafilm with a snap lid. The prepared top glass was attached to the BOFETs substrate to keep the humidity in during electrical measurement. the prepared top glass substrate was placed onto the bottom device substrate.

Fabrication of BOFET and inverters: The poly[2,5-bis(3-tetradecylthiophen-2-yl)thieno[3,2-*b*]thiophene] (PBTTT-C14) (Sigma Aldrich) and 9-Bis(2-methylene-((3-(1,1-dicyanomethylene)-6,7-difluoro)-indanone))-5,5,11,11-tetrakis(4-hexylphenyl)-dithieno [2,3-d:2',3'-d']-s-indaceno[1,2-*b*:5,6-*b*']dithiophene (ITIC-F) (Sigma Aldrich) solution were prepared in chlorobenzene (Sigma Aldrich) with a 5 mg/ mL concentration. A Microfab JETLAB II was manipulated to ink-print each OSC onto the prepared CNC layer through a 40 µm diameter piezoelectric-driven inkjet nozzle, where with an accuracy of 5 µm accuracy movement based on a motorized stage. The resultant OSC channel was ~ 500 × 50 µm^2 with a scanning operation velocity of 1 cm/s, where the burst number of the droplets was ~50. the Au source/drain electrodes (~ 50 nm thickness) were deposited onto the CNC layers by thermal evaporation through a shadow mask under $5.0 × 10^{-6}$ Torr, in which length (L) and width (W) of the active channel was 500 and 50 µm, respectively. By connecting the drain and source from each p- and n-type BOFET with carbon paste, the integrated inverter circuits were demonstrated.

Optoelectrical measurement of BOFETs: The capacitance of the salt-introduced CNC layers as a function of frequency for different humidity conditions was measured by impedance spectroscopy with an LCR meter (4287A, Agilent), where a frequency range was 10 mHz to 0.1 MHz and an AC excitation voltage was 500 mV.

The BOFETs were tested under ambient ambient conditions by utilizing a semiconductor parameter analyzer (4200-SCS, Keithley). For charge carrier mobilities, they were calculated by using the equation under the saturation region:

$$I_{DS} = \left(\frac{WC_i}{2L}\right)\mu(V_{GS} - V_{th})^2 \qquad (3)$$

where C_i is the geometrical capacitance value of the CNC films under different humidity conditions. The threshold voltage (V_{th}) was evaluated by a linear fitting of the transfer curves.

The optoelectrical characterization was performed on the dark and under LED (Thorlabs) illumination conditions ($\sim$ 1 mW cm^{-2}), whose electroluminescence emission peaks were ~ 550 and 730 nm. Before the optoelectrical experiments, the distinct exposed optical powers were evaluated by a Thorlabs 120 UV power sensor. For the real-time V$_{out}$ measurement of the bio-multivalued logic system, different handednesses of CPL exposure were conducted by the experimental sequence of LCPL and RCPL by a rotating linear polarizer, where the rotation of the polarizer 45° clockwise from the crossed polarizer and the quarter-wave plate transmitted the RCPL and vice versa.

Materials Characterization

For the light absorption measurement, free-standing CNC films between quartz slides were analyzed by a Shimadzu UV-3600 spectrometer with the conditioned humidity control chamber for 96 hr. To measure the response of the films to the differently polarized light, the transmission measurement was conducted by using different types of CPL filters such as LCPL, LPL, and RCPL.

CD spectroscopy of an Applied Photophysics Chirascan™-plus was used with the prepared CNC films, where they were placed perpendicularly to the beam direction within a wavelength range (300 ~ 800 nm).

The light tapping mode of AFM was conducted by the ICON Dimension microscope (Bruker) according to the common process.[71] The scan rate and resolution of the evaluation were ~ 0.8 Hz and 512 × 512 pixels, respectively. The AFM tips (MikroMasch, HQ:XSC11/AL BS) showing a nominal tip radius of ~ 10 nm with a spring constant ~ 2.0 N m^{-1} were utilized.

SEM imaging of the CNC film was performed by a Hitachi SU-8230 by introducing a 5 kV accelerating voltage. To obtain the cross-sectional image, a razor blade was utilized to cut the film and it was attached to the SEM mount side by a carbon tape. The Au layer (~ 2 nm) was deposited onto the prepared sample by using sputter technique for ~ 60 s.

Optical microscopy of logic elements in the reflection mode was conducted by an Olympus BX51 microscope.

Acknowledgments

Author contributions

M.J.H. and V.V.T. designed the research; M.J.H. conducted electronic devices measurement; M.K. synthesized and measured optical characteristics of the CNC films; M.J.H. and V.V.T. investigated the experimental results and prepared the manuscript.

Additional information

The authors declare no competing financial interests.

References

[1] Zi, J.; Yu, X.; Li, Y.; Hu, X.; Xu, C.; Wang, X.; Liu, X.; Fu, R. Coloration strategies in peacock feathers. *Proc. Natl. Acad. Sci. U. S. A.* **2003**, *100*, 12576.

[2] Denton, E. Reflectors in Fishes. *Sci Am.* **1971**, *224*, 64–72.

[3] Vignolini, S.; Rudall, P. J.; Rowland, A. V.; Reed, A.; Moyroud, E.; Faden, R. B.; Baumberg, J. J.; Glover, B. J.; Steiner, U. Pointillist Structural Color in *Pollia* Fruit. *Proc. Natl. Acad. Sci. U.S.A.* **2012**, *109*, 15712–15715.

[4] Vaz, R.; Frasco, M. F.; Sales, M. G. F. Photonics in Nature and Bioinspired Designs: Sustainable Approaches for a Colourful World. *Nanoscale Adv.* **2020**, *2*, 5106–5129.

[5] Chiou, T.-H.; Kleinlogel, S.; Cronin, T.; Caldwell, R.; Loeffler, B.; Siddiqi, A.; Goldizen, A.; Marshall, J. Circular Polarization Vision in a Stomatopod Crustacean. *Current Biology* **2008**, *18*, 429–434.

[6] Labhart, T. How polarization-sensitive interneurones of crickets perform at low degrees of polarization. *J. Exp. Biol.* **1996**, *199*, 1467–1475 (1996).

[7] Rossel, S.; Wehner, R. Polarization Vision in Bees. *Nature* **1986**, *323*, 128–131.

[8] Horváth, G., Ed.; *Polarized Light and Polarization Vision in Animal Sciences* (Springer Berlin Heidelberg, Berlin, Heidelberg, 2014; http://link.springer.com/10.1007/978-3-642-54718-8).

[9] Takahashi, Y. K.; Medapalli, R.; Kasai, S.; Wang, J.; Ishioka, K.; Wee, S. H.; Hellwig, O.; Hono, K.; Fullerton, E. E. Accumulative Magnetic Switching of Ultrahigh-Density Recording Media by Circularly Polarized Light. *Phys. Rev. Applied* **2016**, *6*, 054004.

[10] Grell, M.; Oda, M.; Whitehead, K. S.; Asimakis, A.; Neher, D.; Bradley, D. D. C. A Compact Device for the Efficient, Electrically Driven Generation of Highly Circularly Polarized Light. *Adv. Mater.* **2001**, *13*, 577–580.

[11] Gilot, J.; Abbel, R.; Lakhwani, G.; Meijer, E. W.; Schenning, A. P. H. J.; Meskers, S. C. J. Polymer Photovoltaic Cells Sensitive to the Circular Polarization of Light. *Adv. Mater.* **2010**, *22*, E131–E134.

[12] Richtberg, S.; Girwidz, R. Use of Linear and Circular Polarization: The Secret LCD Screen and 3D Cinema. *The Physics Teacher* **2017**, *55*, 406–408.

[13] Miyamoto, K.; Wortelen, H.; Okuda, T.; Henk, J.; Donath, M. Circular-Polarized-Light-Induced Spin Polarization Characterized for the Dirac-Cone Surface State at W(110) with C2v Symmetry. *Sci Rep* **2018**, *8*, 10440.

[14] Liu, H.; Li, Q.; Bu, Y.; Zhang, N.; Wang, C.; Pan, C.; Mi, L.; Guo, Z.; Liu, C.; Shen, C. Stretchable Conductive Nonwoven Fabrics with Self-Cleaning Capability for Tunable Wearable Strain Sensor. *Nano Energy* **2019**, *66*, 104143.

[15] Herzer, N.; Guneysu, H.; Davies, D. J. D.; Yildirim, D.; Vaccaro, A. R.; Broer, D. J.; Bastiaansen, C. W. M.; Schenning, A. P. H. J. Printable Optical Sensors Based on H-Bonded Supramolecular Cholesteric Liquid Crystal Networks. *J. Am. Chem. Soc.* **2012**, *134*, 7608–7611.

[16] Stumpel, J. E.; Gil, E. R.; Spoelstra, A. B.; Bastiaansen, C. W. M.; Broer, D. J.; Schenning, A. P. H. J. Stimuli-Responsive Materials Based on Interpenetrating Polymer Liquid Crystal Hydrogels. *Adv. Funct. Mater.* **2015**, *25*, 3314–3320.

[17] Deng, Z.; Zhou, G.; de Haan, L. T. Preparation of an Interpenetrating Network of a Poly(Ampholyte) and a Cholesteric Polymer and Investigation of Its Hydrochromic Properties. *ACS Appl. Mater. Interfaces* **2019**, *11*, 36044–36051.

[18] Zhang, Z.-H.; Zhang, J.-W.; Cao, C.-F.; Guo, K.-Y.; Zhao, L.; Zhang, G.-D.; Gao, J.-F.; Tang, L.-C. Temperature-responsive resistance sensitivity controlled by L-ascorbic acid and silane co-functionalization in flame-retardant GO network for efficient fire early-warning response. *Chem. Engineering Journal.* **2020**, *386*, 123894.

[19] Liu, X.; Wang, R.; Zhang, T.; He, Y.; Tu, J.; Li, X. Synthesis and Characterization of Mesoporous Indium Oxide for Humidity-Sensing Applications. *Sensors and Actuators B: Chemical* **2010**, *150*, 442–448.

20 Mohd-Noor, S.; Jang, H.; Baek, K.; Pei, Y.-R.; Alam, A.-M.; Kim, Y. H.; Kim, I. S.; Choy, J.-H.; Hyun, J. K. Ultrafast Humidity-Responsive Structural Colors from Disordered Nanoporous Titania Microspheres. *J. Mater. Chem. A* **2019**, *7*, 10561–10571.

21 Hu, W.; Chen, M.; Wang, Q.; Zhang, L.; Yuan, X.; Chen, F.; Yang, H. Broadband Reflection in Polymer-Stabilized Cholesteric Liquid Crystals via Thiol–Acrylate Chemistry. *Angew. Chem. Int. Ed.* **2019**, *58*, 6698–6702.

22 Kragt, A. J. J.; Broer, D. J.; Schenning, A. P. H. J. Easily Processable and Programmable Responsive Semi-Interpenetrating Liquid Crystalline Polymer Network Coatings with Changing Reflectivities and Surface Topographies. *Adv. Funct. Mater.* **2018**, *28*, 1704756.

23 Shopsowitz, K. E.; Qi, H.; Hamad, W. Y.; MacLachlan, M. J. Free-Standing Mesoporous Silica Films with Tunable Chiral Nematic Structures. *Nature* **2010**, *468*, 422–425.

24 Kose, O.; Tran, A.; Lewis, L.; Hamad, W. Y.; MacLachlan, M. J. Unwinding a Spiral of Cellulose Nanocrystals for Stimuli-Responsive Stretchable Optics. *Nat Commun* **2019**, *10*, 510.

25 Xiong, R.; Luan, J.; Kang, S.; Ye, C.; Singamaneni, S.; Tsukruk, V. V. Biopolymeric Photonic Structures: Design, Fabrication, and Emerging Applications. *Chem. Soc. Rev.* **2020**, *49*, 983–1031.

26 Xiong, R.; Yu, S.; Kang, S.; Adstedt, K. M.; Nepal, D.; Bunning, T. J.; Tsukruk, V. V. Integration of Optical Surface Structures with Chiral Nanocellulose for Enhanced Chiroptical Properties. *Adv. Mater.* **2020**, *32*, 1905600.

27 Tardy, B. L.; Richardson, J. J.; Greca, L. G.; Guo, J.; Ejima, H.; Rojas, O. J. Exploiting Supramolecular Interactions from Polymeric Colloids for Strong Anisotropic Adhesion between Solid Surfaces. *Adv. Mater.* **2020**, *32*, 1906886.

28 Sun, C.; Zhu, D.; Jia, H.; Lei, K.; Zheng, Z.; Wang, X. Humidity and Heat Dual Response Cellulose Nanocrystals/Poly(*N*-Isopropylacrylamide) Composite Films with Cyclic Performance. *ACS Appl. Mater. Interfaces* **2019**, *11*, 39192–39200.

29 Chen, H.; Hou, A.; Zheng, C.; Tang, J.; Xie, K.; Gao, A. Light- and Humidity-Responsive Chiral Nematic Photonic Crystal Films Based on Cellulose Nanocrystals. *ACS Appl. Mater. Interfaces* **2020**, *12*, 24505–24511.

30 Boott, C. E.; Tran, A.; Hamad, W. Y.; MacLachlan, M. J. Cellulose Nanocrystal Elastomers with Reversible Visible Color. *Angew. Chem.* **2020**, *132*, 232–237.

31 Chen, T.; Zhao, Q.; Meng, X.; Li, Y.; Peng, H.; Whittaker, A. K.; Zhu, S. Ultrasensitive Magnetic Tuning of Optical Properties of Films of Cholesteric Cellulose Nanocrystals. *ACS Nano* **2020**, *14*, 9440–9448.

32 Kang, S.; Li, Y.; Bukharina, D.; Kim, M.; Lee, H.; Buxton, M. L.; Han, M. J.; Nepal, D.; Bunning, T. J.; Tsukruk, V. V. Bio-Organic Chiral Nematic Materials with Adaptive Light Emission and On-Demand Handedness. *Adv. Mater.* **2021**, *33*, 2103329.

33 Kim, M.; Lee, H.; Krecker, M. C.; Bukharina, D.; Nepal, D.; Bunning, T. J.; Tsukruk, V. V. Switchable Photonic Bio-Adhesive Materials. *Adv. Mater.* **2021**, *33,* 2103674.

34 Habibi, Y.; Lucia, L. A.; Rojas, O. J. Cellulose Nanocrystals: Chemistry, Self-Assembly, and Applications. *Chem. Rev.* **2010**, *110*, 3479–3500.

35 Wan, H.; Li, X.; Zhang, L.; Li, X.; Liu, P.; Jiang, Z.; Yu, Z.-Z. Rapidly Responsive and Flexible Chiral Nematic Cellulose Nanocrystal Composites as Multifunctional Rewritable Photonic Papers with Eco-Friendly Inks. *ACS Appl. Mater. Interfaces* **2018**, *10*, 5918–5925.

36 Edgar, C. D.; Gray, D. G. Induced Circular Dichroism of Chiral Nematic Cellulose Films. *Cellulose* **2001**, *8*, 5.

37 Dong, X. M.; Kimura, T.; Revol, J.-F.; Gray, D. G. Effects of Ionic Strength on the Isotropic−Chiral Nematic Phase Transition of Suspensions of Cellulose Crystallites. *Langmuir* **1996**, *12*, 2076–2082.

38 Carey, T.; Cacovich, S.; Divitini, G.; Ren, J.; Mansouri, A.; Kim, J. M.; Wang, C.; Ducati, C.; Sordan, R.; Torrisi, F. Fully Inkjet-Printed Two-Dimensional Material Field-Effect Heterojunctions for Wearable and Textile Electronics. *Nat Commun* **2017**, *8*, 1202.

39 Fang, X.; Shi, J.; Zhang, X.; Ren, X.; Lu, B.; Deng, W.; Jie, J.; Zhang, X. Patterning Liquid Crystalline Organic Semiconductors via Inkjet Printing for High-Performance Transistor Arrays and Circuits. *Adv. Funct. Mater.* **2021**, *31*, 2100237.

40 Persson, N. E.; McBride, M. A.; Grover, M. A.; Reichmanis, E. Automated analysis of orientational order in images of fibrillar materials. *Chem. Mater.* 2016, *29*, 3–14.

41 de Vries, Hl. Rotatory power and other optical properties of certain liquid crystals. *Acta Cryst* **1951**, *4,* 219–226.

42 Wang, P.-X.; Hamad, W. Y.; MacLachlan, M. J. Structure and Transformation of Tactoids in Cellulose Nanocrystal Suspensions. *Nat Commun* **2016**, *7*, 11515.

43 Cunha, I.; Barras, R.; Grey, P.; Gaspar, D.; Fortunato, E.; Martins, R.; Pereira, L. Reusable Cellulose-Based Hydrogel Sticker Film Applied as Gate Dielectric in Paper Electrolyte-Gated Transistors. *Adv. Funct. Mater.* **2017**, *27*, 1606755.

44 Kim, M.; Pierce, K.; Krecker, M.; Bukharina, D.; Adstedt, K.; Nepal, D.; Bunning, T.; Tsukruk, V. V. Monolithic Chiral Nematic Organization of Cellulose Nanocrystals under Capillary Confinement. *ACS Nano* **2021**, *15*, 19418–19429.

45 Kim, M.; Lee, H.; Snipes, R. T.; Han, M. J.; Tsukruk, V. V. Co-Assembly of Biosynthetic Chiral Nematic Adhesive Materials with Dynamic Polarized Luminescence. *Small* **2022**, *18*, 2104340.

46 Albano, G.; Pescitelli, G.; Di Bari, L. Chiroptical Properties in Thin Films of π-Conjugated Systems. *Chem. Rev.* **2020**, *120*, 10145−10243.

47 Han, H.; Lee, Y. J.; Kyhm, J.; Jeong, J. S.; Han, J. H.; Yang, M. K.; Lee, K. M.; Choi, Y.; Yoon, T. H.; Ju, H.; Ahn, S. k.; Lim, J. A. High-Performance Circularly Polarized Light-Sensing Near-Infrared Organic Phototransistors for Optoelectronic Cryptographic Primitives. *Adv. Funct. Mater.* **2020**, *30*, 2006236.

48 Cheng, J.; Ge, F.; Xiang, Y.; Zhang, H.; Kuai, Y.; Hou, P.; Zhang, D.; Qiu, L.; Zhang, Q.; Zou, G. Induction of Circularly Polarized Electroluminescence from Achiral Poly(fluorene-alt-benzothiadiazole) by Circularly Polarized Light. *J. Mater. Chem. C* **2020**, *8*, 6521– 6527.

49 Lee, J.; Park, J.-S.; Pyo, Y. S.; Lee, D. B.; Kim, E. H.; Stryakhilev, D.; Kim, T. W.; Jin, D. U.; Mo, Y.-G. The influence of the gate dielectrics on threshold voltage instability in amorphous indium-gallium-zinc oxide thin film transistors. *Appl. Phys. Lett.* **2009**, *95*, 123502.

50 Liu, L.-C.; Chen, J.-S.; Jeng, J.-S. Role of Oxygen Vacancies on the Bias Illumination Stress Stability of Solution-processed Zinc Tin Oxide Thin Film Transistors. *Appl. Phys. Lett.* **2014**, *105*, 023509.

51 Qu, M.; Li, H.; Liu, R.; Zhang, S. L.; Qiu, Z. J. Interaction of Bipolaron with the H_2O/O_2 Redox Couple Causes Current Hysteresis in Organic Thin-Film Transistors *Nat. Commun.* **2014**, *5*, 3185.

52 Aguirre, C. M.; Levesque, P. L.; Paillet, M.; Lapointe, F.; St-Antoine, B. C.; Desjardins, P.; Martel, R. The Role of the Oxygen/water Redox Couple in Suppressing Electron Conduction in Field-Effect Transistors *Adv. Mater.* **2009**, *21*, 3087– 3091.

53 Yang, K.; Yuan, S.; Qiu, Z.; Zhan, Y; Umar, A. A.; Zheng, L.; Seoane, F. Humidity effect on photoelectrical properties of photosensitive field effect transistors. *Org. Electron.* **2019**, *69*, 42–47.

54 Kim, H.; Kim, G.; Song, I.; Lee, J.; Abdullah, H.; Yang, C.; Oh, J. H. Ambipolar Organic Phototransistors Based on 6,6′-dibromoindigo. *RSC Adv.* **2018**, *8*, 14747– 14752.

55 Labram, J. G.; Wöbkenberg, P. H.; Bradley, D. D. C.; Anthopoulos, T. D. Low-Voltage Ambipolar Phototransistors Based on a Pentacene/PC61BM Heterostructure and a Self-Assembled Nano-Dielectric. *Org. Electron.* **2010**, *11*, 1250–1254.

56 He, J.; Xiao, P.; Shi, J.; Liang, Y.; Lu, W.; Chen, Y.; Wang, W.; Théato, P.; Kuo, S.-W.; Chen, T. High Performance Humidity Fluctuation Sensor for Wearable Devices via a Bioinspired Atomic-Precise Tunable Graphene-Polymer Heterogeneous Sensing Junction. *Chem. Mater.* **2018**, *30*, 4343–4354.

57 Lee, J.-U.; Ma, Y.-W.; Jeong, S.-Y.; Shin, B.-S. Direct Fabrication of Ultra-Sensitive Humidity Sensor Based on Hair-Like Laser-Induced Graphene Patterns. *Micromachines* **2020**, *11*, 476.

58 Li, Z.; Wang, J.; Xu, Y.; Shen, M.; Duan, C.; Dai, L.; Ni, Y. Green and Sustainable Cellulose-Derived Humidity Sensors: A Review. *Carbohydrate Polymers* **2021**, *270*, 118385.

59 Zhao, T. H.; Parker, R. M.; Williams, C. A.; Lim, K. T. P.; Frka-Petesic, B.; Vignolini, S. Printing of Responsive Photonic Cellulose Nanocrystal Microfilm Arrays. *Adv. Funct. Mater.* **2019**, *29*, 1804531.

[60] Lu, T.; Pan, H.; Ma, J.; Li, Y.; Bokhari, S. W.; Jiang, X.; Zhu, S.; Zhang, D. Cellulose Nanocrystals/Polyacrylamide Composites of High Sensitivity and Cycling Performance To Gauge Humidity. *ACS Appl. Mater. Interfaces* **2017**, *9*, 18231–18237.

[61] Han, M. J.; Kim, M.; Tsukruk, V. V. Multivalued Logic for Optical Computing with Photonically Enabled Chiral Bio-organic Structures. *ACS Nano*, **2022**, *16*, 13684–13694.

[62] Fang, X.; Ren, H.; Gu, M. Orbital Angular Momentum Holography for High-Security Encryption. *Nat. Photonics* **2020**, *14*, 102–108.

[63] Zheng, P.; Dai, Q.; Li, Z.; Ye, Z.; Xiong, J.; Liu, H. C.; Zheng, G.; Zhang, S. Metasurface-based key for computational imaging encryption. *Sci. Adv.* **2021**, *7*, eabg0363.

[64] Tan, J.; Li, Q.; Meng, S.; Li, Y.; Yang, J.; Ye, Y.; Tang, Z.; Qu, S.; Ren, X. Time-Dependent Phosphorescence Colors from Carbon Dots for Advanced Dynamic Information Encryption. *Adv. Mater.* **2021**, *33*, 2006781.

[65] Bennett, C. H. Quantum cryptography using any two nonorthogonal states. *Phys. Rev. Lett.* **1992**, *68,* 3121–3124.

[66] Kak, S.; Verma, P.; MacDonald, G. in (Eds.: C. Roychoudhuri, A. Yu. Khrennikov, A. F. Kracklauer), San Diego, California, USA, 2011, p. 81210M.

[67] Zhou, H.; Sain, B.; Wang, Y.; Schlickriede, C.; Zhao, R.; Zhang, X.; Wei, Q.; Li, X.; Huang, L.; Zentgraf, T. Polarization-Encrypted Orbital Angular Momentum Multiplexed Metasurface Holography. *ACS Nano* **2020**, *14*, 5553–5559.

[68] Kim, J.; Jeon, D.; Seong, J.; Badloe, T.; Jeon, N.; Kim, G.; Kim, J.; Baek, S.; Lee, J.-L.; Rho, J. Photonic Encryption Platform via Dual-Band Vectorial Metaholograms in the Ultraviolet and Visible. *ACS Nano* *2022, 16*, 3546–3553.

[69] Beck-Candanedo, S.; Roman, M.; Gray, D. G. Effect of Reaction Conditions on the Properties and Behavior of Wood Cellulose Nanocrystal Suspensions. *Biomacromolecules* **2005**, *6*, 1048–1054.

[70] Greenspan, L. Humidity fixed points of binary saturated aqueous solutions. *Sect. A*. 1977, **81A**, 89.

[71] McConney, M. E.; Singamaneni, S.; Tsukruk, V. V. Probing Soft Matter with the Atomic Force Microscopies: Imaging and Force Spectroscopy. *Polym. Rev.* **2010**, *50*, 235–286.